

Giant earthquakes on quiet faults governed by rheological transitions

Martijn P.A. van den Ende^{*1,2}, Jianye Chen¹, Jean-Paul Ampuero^{2,3} and André R. Niemeijer¹

1 **The apparent stochastic nature of earthquakes poses major challenges for earthquake forecasting attempts.**
2 **Physical constraints on the seismogenic potential of major fault zones may aid in improving seismic hazard**
3 **assessments, but the mechanics of earthquake nucleation and rupture are obscured by the complexity**
4 **that faults display. In this work, we investigate the mechanisms behind giant earthquakes by employing**
5 **a microphysically based seismic cycle simulator. This microphysical approach is directly based on the**
6 **mechanics of friction as inferred from laboratory tests, and can explain a broad spectrum of fault slip**
7 **behaviour. We show that regular earthquakes are controlled by the size and distribution of nominally**
8 **unstable asperities, whereas fault-spanning earthquakes are governed by a rheological transition occurring**
9 **in creeping fault segments. Moreover, this facilitates the nucleation of giant earthquakes on faults that**
10 **are weakly seismically coupled. This microphysically based approach offers opportunities for investigating**
11 **long-term seismic cycle behaviour of natural faults.**

12 One major limitation of seismic hazard assessments is that they are mostly based on statistics rather than
13 physics. Particularly for large earthquakes that have recurrence times of up to several centuries, instrumental
14 catalogues of seismic events in a given region are short or absent, so that statistical analyses can only be
15 performed through the extrapolation of smaller, more frequent events, which entails model assumptions that
16 are difficult to test. Constraints originating from a physical understanding of earthquakes may therefore greatly
17 improve seismic hazard assessments, but basic underlying mechanisms are obscured by the enormous complexity
18 inherent to natural fault zones.

19 Over the last two decades or so, innovative techniques in palaeoseismology have substantially expanded
20 our catalogue of (pre)historic seismic events, revealing earthquake supercycles in the form of spatio-temporal
21 clustering of earthquakes¹⁻⁴ and occurrences of exceptionally large events ('superimposed cycles')⁵⁻⁸. In
22 addition, millenary recurrence of $M_w \geq 9.0$ earthquakes has been anticipated for the Main Himalayan Thrust⁹
23 and Japan Trench¹⁰ regions on the basis of geodetic estimates of moment accumulation rates. These inferences
24 suggest that the lack of instrumental recordings of great ($M_w > 8$) and giant ($M_w > 9$) earthquakes does
25 not imply an intrinsic upper limit of event magnitude. The 2004 Sumatra-Andaman and 2011 Tohoku-Oki
26 $M_w > 9$ events, hosted by subduction thrusts that were previously marked in hazard maps as being incapable
27 of generating such large magnitude events¹⁰⁻¹², are exemplary to this notion. Statistical analyses of earthquake
28 catalogues do not exclude that most (if not all) subduction regions are intrinsically capable of hosting giant
29 earthquakes^{13,14}, provided that the seismogenic zone geometry is not restrictive (e.g. Weng & Yang¹⁵).

¹High Pressure and Temperature Laboratory, Department of Earth Sciences, Utrecht University, the Netherlands

²Université Côte d'Azur, IRD, CNRS, Observatoire de la Côte d'Azur, Géoazur, France

³Seismological Laboratory, California Institute of Technology, Pasadena, CA, USA

30 The occurrence of great earthquakes in all subduction settings is suggestive of a common underlying
31 mechanism. On the other hand, though numerous subduction regions have been identified to host giant
32 earthquakes, some of these regions presently exhibit high seismicity rates (Japan Trench⁸, Sumatra⁴), while
33 other megathrusts are currently quiescent except for deeper slow slip and tremor (Alaska¹⁶, Cascadia¹⁷), or
34 generally display low levels of background seismicity (Andaman, Chile Maule¹⁸). This geographical variability
35 in seismic character requires that the mechanism for the generation of giant earthquakes is at least partly
36 independent of that of regular earthquakes, allowing great and giant earthquakes to occur in both seismically
37 active and quiet regions. Furthermore, seismological and numerical evidence suggests that creeping (weakly
38 seismically coupled) fault segments may host propagation of dynamic ruptures^{19–21}, even though creeping
39 segments are generally thought to impede fast rupture events²². To elucidate the emergence of giant earthquakes
40 that inevitably propagate through (or possibly nucleate within) creeping fault segments, the underlying physical
41 mechanisms of fault rock deformation need to be closely considered.

42 **A microphysically based approach for earthquake modelling**

43 The seismic cycle behaviour of (heterogeneous) faults has been explored in numerical studies^{22–25}, most
44 commonly employing the rate-and-state friction²⁶ (RSF) formulation as a description for the time- and
45 velocity-dependence of fault strength (see Supplementary Information S1). While the classical RSF framework
46 is originally motivated by laboratory observations²⁷, it is empirical in nature, and so provides limited physical
47 basis for the extrapolation of laboratory results to natural scales and conditions. Most importantly, the RSF
48 model parameters are typically assumed to be independent of fault slip velocity, whereas much laboratory
49 evidence suggests a more complex velocity-dependence of friction^{28–32}. Since the fault slip velocity likely varies
50 by over 10 orders of magnitude over the course of a seismic cycle, the assumption of constant values of the RSF
51 constitutive parameters greatly impacts the transient slip and nucleation behaviour, as seen in seismic cycle
52 simulations³³.

53 As an alternative approach, microphysical models allow for an interpretation of their parameters in terms of
54 thermodynamic or material quantities, such as temperature, fault gouge nominal grain size, or solubility of the
55 solid phase^{34,35}. This facilitates the generalisation of complex laboratory behaviour, and the extrapolation of
56 laboratory results to natural scales and conditions with an independent assessment of the validity of the model
57 outcomes. Most commonly, microphysical descriptions of (steady-state) fault rheology are based on plastic creep
58 of contact asperities between bare rock interfaces, motivated by metallurgical and tribological studies of friction
59 of metals (e.g. refs^{36–38}; Supplementary Information S2). Such models do not, however, fully acknowledge the
60 complex granular dynamics of fault gouges and corresponding deformation mechanisms observed in laboratory
61 experiments and in field studies (see Supplementary Information S3). In this study, we employ the *Chen-*
62 *Niemeijer-Spiers* (CNS) model^{34,39}, which specifically considers the deformation of fault gouges, and is seated
63 on laboratory and field observations. Previous work³³ has demonstrated how the implementation of the CNS
64 model into the seismic cycle simulator QDYN⁴⁰, is capable of producing a range of fault slip behaviours
65 previously ascribed only to rate-and-state friction, while maintaining a clear physical interpretation. In its

66 essence, the CNS microphysical model considers the interplay between a time-dependent compaction mechanism
67 (pressure solution creep), and dilatant granular flow (see Methods). Both these micro-mechanisms have been
68 identified to be highly relevant for fault rock deformation at seismogenic zone conditions^{32,41–45}. Because
69 the microphysical principles for the CNS model are based on a wide range of laboratory^{30,34,39} and field^{46,47}
70 observations, the model outcomes are readily understood in terms of micro-scale observable quantities.

71 By using a microphysical model for describing the fault rheology, one can readily incorporate field and
72 laboratory observations into a numerical seismic cycle simulator³³. Following numerous field studies of
73 exhumed fault zones, we distinguish between two types of fault rock (Fig. 1 and Supplementary Information
74 S3): a phyllite-mylonite matrix deforming predominantly by pressure solution creep, and gouge derived from
75 “competent” lenses (competence defined at the imposed strain rate) that exhibits both pressure solution creep
76 and granular flow. In analogy to seismogenic asperities identified by seismological studies, we refer to fault
77 segments associated with competent lenses as asperities. These asperities obey a fractal distribution in size
78 and separation distance (c.f. Fagereng⁴¹), adding to the complexity of heterogeneous faults. To address this
79 complexity, simplifications have to be made regarding the architecture of the fault in order to reduce the highly
80 complex fault zone structure to one that is numerically feasible (see Fig. 1a). As a first-order representation, we
81 simulate a one-dimensional, along-strike fault line that cuts through the fault zone, alternatingly encountering
82 one of the two end-member types of fault rock defined above (i.e. the matrix or the gouge). This produces
83 an alternating pattern of phyllosilicate matrix and asperity-derived gouge (see the “Idealisation” in Fig. 1a),
84 characterised by a fractal dimension D and occupation ratio f – see also the *Methods* section. One important
85 drawback of this procedure is that the details of the volumetric distribution of deformation are lost, and so the
86 model remains unconstrained in the strain rate accommodated within the fault zone.

87 The CNS model envisions a microstructure that is representative of a gouge consisting predominantly of
88 structure-forming minerals like quartz or calcite. While this assumed geometry holds for the asperity-derived
89 gouges, it does not fully capture the microstructure of the phyllosilicate-dominated matrix segments. However,
90 microphysical models³⁵ that consider a geometry that is more appropriate for the matrix, predict similar trends
91 in fault rheology as does the CNS model via the same micro-scale mechanisms (i.e. non-dilatant creep by
92 pressure solution and dilatation by granular flow), the main difference lying in geometric parameters derived
93 from the model geometry. We therefore take the CNS model to describe the rheology of both the matrix and
94 gouge segments. The compositional distinction between the two types is made through a contrast in pressure
95 solution kinetics, with the matrix exhibiting faster pressure solution kinetics than the asperities (Fig. 1b) as
96 suggested by field observations⁴¹ and by experiments conducted on halite-phyllite interfaces⁴⁸.

97 We consider a set of conditions typical for subduction zones at seismogenic depths with temperature
98 $T = 250\text{ }^\circ\text{C}$, far-field driving velocity $V_{imp} = 10^{-9}\text{ m/s}$ ($\approx 30\text{ mm/yr}$), and effective normal stress $\sigma = 50\text{ MPa}$
99 (although no consensus exists on the average magnitude of the fluid pressure, leaving great uncertainty in
100 the value of σ). At steady-state deformation under these conditions, the matrix deforms predominantly by
101 velocity-strengthening ductile creep, whereas the asperities deform by parallel operation of pressure solution and

102 granular flow, producing velocity-weakening behaviour³⁹. However, in the seismic cycle simulations deformation
103 occurs under non-steady state conditions, resulting in a spectrum of fault slip transients³³ governed by the
104 rheological model. Following the procedure described in the Methods section, we simulate 2000 years of slip
105 along the strike of a heterogeneous, one-dimensional periodic fault (under the a “2.5D” approximation), with an
106 along-strike length of 16 km (Fig. 1a), and investigate emergent transient slip features. Although the dimensions
107 of the model fault are smaller than those typical for megathrusts, the outcomes of the numerical simulations
108 are interpreted in a general framework suitable for up-scaling.

109 **Emergence of giant earthquakes**

110 Slip distribution maps for all 10 simulations (with various combinations of fractal dimension D and asperity
111 occupation f) are given in Supplementary Information S4. Examples of characteristic fault slip behaviour
112 produced in the simulations are given in Fig. 2a. Sections on the fault that exhibit a high asperity density
113 display repeated seismic activity, rupturing small clusters of closely-spaced asperities in a single event. Dynamic
114 ruptures are arrested by regions consisting predominantly of ductile matrix, so that separated clusters of
115 asperities remain mostly isolated. Motivated by Luo & Ampuero²⁴, we classify this type of events as partial
116 or P-instabilities, defined as an instability that ruptures only a portion of the entire fault. Note that, unlike
117 Luo & Ampuero²⁴, P-events may encompass several (clusters) of nominally velocity-weakening asperities. The
118 seismic character of the simulation (i.e. maximum slip velocities during P-instabilities) seems largely controlled
119 by the fractal dimension D of the asperity size distribution: simulations with $D = 1$ (dominated by several large
120 asperities) show P-instabilities that attain coseismic slip rates, whereas simulations with $D = 2$ (dominated by
121 numerous small asperities) only exhibit aseismic P-instabilities in the form of small slow slip events, consistent
122 with geological observations⁴¹.

123 In addition to these P-events, the fault occasionally hosts seismic events that rupture the full extent of the
124 fault, reaching coseismic slip velocities even in regions dominated by ductile matrix. This second class of seismic
125 events is referred to as (“total”) T-instabilities. The occurrence of T-events is not restricted to simulations
126 with seismic P-instabilities, as T-instabilities are also produced in simulations that otherwise only exhibit small
127 slow slip events (which would likely remain undetected by surface monitoring stations). Aside from the seismic
128 character of the model fault, the value of D also affects the style of nucleation⁴⁹ of the T-instabilities, with a
129 cascade-up mode of nucleation observed in simulations with $D = 1$, and a preslip (or “own nucleation”) mode
130 observed in simulations with $D = 2$ (see Fig. 2a).

131 Extending these observations to natural fault zones, one can draw an analogy between P-events, being
132 controlled by a local asperity distribution of nominally velocity-weakening material, and regular natural
133 earthquakes. The T-instabilities generated in the simulations may find their natural counterpart in multi-
134 segment ruptures and anomalously large events ($M_w > 9$), as appearing in palaeoseismic records^{5,6}. It is most
135 striking that simulated faults that exhibit weak seismic coupling over their entire extent and that are otherwise
136 seismically quiet are also capable of generating T-instabilities. This shows that the mechanisms and conditions
137 for generating T-events are different from those for P-events. Furthermore, these simulations demonstrate that

138 creeping fault segments may also host or nucleate seismic ruptures, instead of quenching or impeding dynamic
139 ruptures²².

140 **Microphysical mechanisms behind giant earthquakes**

141 More insight into the emergence of T-instabilities is gained by considering the time-evolution of average fault
142 stress (Fig. 2b). In simulations that exhibit a fractal dimension $D = 1$, the average shear stress supported by
143 the asperities remains roughly constant over time, whereas the average stress on the matrix increases between
144 subsequent T-instabilities, so that the net fault stress increases over time. At a critical value of stress, a
145 T-instability is generated. In the simulations with $D = 2$, the stress is more homogeneously distributed, and
146 the stress supported by both the asperities and the matrix segments follows a similar upward trajectory, until
147 a critical stress is reached and a T-instability nucleates. For $D = 2$, the fault behaves similar to one exhibiting
148 homogeneous frictional properties.

149 The occurrence of a fault-spanning instability at a critical stress level can now be explained by a rheological
150 transition predicted by the CNS model, and is illustrated in Fig. 3. At a given moment in time early in a
151 T-cycle, a segment of ductile matrix is deforming by steady-state, non-dilatant pressure solution creep (point 1
152 in Fig. 3). By continuous tectonic loading and non-uniform fault slip, the average stress supported by the
153 matrix increases over time (point 2). The kinetics of pressure solution assigned to the matrix segments are such
154 that at steady-state (i.e. at the far-field driving velocity), the matrix can accommodate the imposed strain rate
155 entirely by ductile creep. In the absence of interactions with the asperities on the fault, the matrix would remain
156 nominally stable (see inset in Fig. 3). However, stress perturbations resulting from mechanical interactions with
157 the asperities may raise the stress acting on a given matrix segment up to a critical value that marks the onset
158 of dilatant granular flow (point 3 in Fig. 3). If a sufficient volume of matrix is critically stressed, a T-instability
159 is triggered in which both the asperities and the matrix segments enter the unstable granular flow regime
160 (point 4). A fault-spanning rupture then results as the entire fault has become unstable. This kind of “mode
161 switching”⁵⁰ has previously been identified in laboratory experiments^{51,52} and in numerical simulations²⁰ at
162 coseismic slip rates (~ 1 m/s), but not at slip rates relevant for the nucleation stage ($\sim 10^{-9}$ m/s).

163 As compared to previous studies considering spatially heterogeneous faults (e.g. refs 23,53–55), the
164 mechanism for generating fault-spanning events is similar in many respects: while the overall state of stress on
165 a fault resides below a critical level, small (partial) ruptures break portions of the fault. As the stress state of
166 the fault approaches criticality, nucleation of a fault-spanning event is permitted. In all of the aforementioned
167 studies, the simulated fault was taken to be intrinsically unstable (i.e. velocity-weakening friction within the
168 seismogenic domain), facilitating dynamic ruptures over the full extent of the fault. By contrast, in the present
169 study the matrix material (which occupies 50% of the fault) shows strong velocity-strengthening behaviour
170 at the imposed loading rate, with the equivalent rate-and-state friction ($a - b$) parameter assuming a value
171 of the order of 0.5³³. Following Kaneko et al.²², such a large value of ($a - b$) would allow a single matrix
172 segment of merely 160 m in length to fully arrest a 16 km long rupture (assuming an average coseismic stress
173 drop of 10 MPa) in the absence of a transition into the velocity-weakening regime. Hence, the rheological

174 transition proposed here is a requirement for nucleating and dynamically propagating fault-spanning events
 175 on compositionally heterogeneous faults. This has further implications for the interpretation of laboratory
 176 friction tests performed under in-situ conditions (e.g. Niemeijer & Vissers⁴⁶), as measurements of strong
 177 velocity-strengthening behaviour cannot a-priori exclude the possibility of nucleation or propagation of dynamic
 178 ruptures. Lastly, in previous studies where heterogeneous frictional parameters were adopted^{23,53-55}, the
 179 simulated faults were always observed to be seismically active in between fault-spanning events, whereas our
 180 simulations with $D = 2$ are seismically quiet and weakly coupled (see Fig. 2a), implying that purely creeping
 181 faults are nonetheless prone to T-instabilities.

182 It is noteworthy that this rheological transition predicted by the CNS microphysical model has been
 183 observed in various materials in laboratory experiments^{30-32,56}. This transition is commonly known as the
 184 brittle-ductile⁵⁷, or flow-to-friction⁵⁸ transition. The outcomes of the numerical simulations are therefore
 185 not a mere peculiarity unique to the adopted fault rheology, and it is expected that models that feature
 186 such brittle-ductile transition (e.g. Den Hartog & Spiers³⁵ and Noda & Shimamoto⁵⁹) will also display an
 187 emergence of T-instabilities due to a stress-driven rheological transition. While such a transition can be
 188 enforced within the current rate-and-state friction framework (e.g. Beeler⁶⁰), microphysical models from which
 189 the brittle-ductile transition naturally emerges are more appealing than purely empirical flow-to-friction laws,
 190 as they can be extrapolated based on measurable material properties, and thereby have stronger predictive
 191 capabilities. Moreover, the use of a microphysical model facilitates the incorporation of laboratory and field
 192 observations into numerical modelling efforts, which further promotes the participation of these disciplines in
 193 physically-based earthquake hazard assessments.

194 Methods

195 **Description of the microphysical model.** The derivation of the CNS model, the comparison with classical rate-and-state
 196 friction, and its implementation into QDYN are described in detail in refs^{33,34,39,61,62}. Some key concepts of this model are
 197 recited here.

198 The CNS model geometry is based on the microstructural observations provided by ref. 30, and considers a granular gouge
 199 layer of uniform thickness h , characterised by a nominal grain size d and porosity ϕ . A representative volume element is subjected
 200 to an effective normal stress σ and deformation rate V_{imp} , which is accommodated internally by parallel operation of granular flow
 201 (grain rolling and sliding), and one or more thermally-activated, time-dependent deformation mechanisms. Following previous
 202 work^{33,34,39} and based on the observations summarised in Supplementary Information S3, we take intergranular pressure solution
 203 as the sole time-dependent mechanism, ignoring other mechanisms such as stress corrosion cracking^{63,64}. The constitutive relation
 204 for the rheology of the fault then results from the individual constitutive relations for granular flow and pressure solution, which
 205 are dependent on the instantaneous state of stress and gouge porosity.

206 For intergranular pressure solution, the flow law for dissolution controlled pressure solution creep is given as^{65,66}:

$$\dot{\gamma}_{ps} = A \frac{I_s \Omega}{RT} \frac{\tau}{d} f_1(\phi) \quad (1a)$$

$$\dot{\epsilon}_{ps} = A \frac{I_s \Omega}{RT} \frac{\sigma}{d} f_2(\phi) \quad (1b)$$

207 Here, $\dot{\gamma}_{ps}$ and $\dot{\epsilon}_{ps}$ are the strain rates in the fault tangential and normal directions, respectively, A is a geometric factor accounting
 208 for the grain shape, I_s is the dissolution rate constant, Ω is the molar volume, R is the universal gas constant, T is the absolute

209 temperature, and τ and σ are the macroscopic shear and effective normal stress, respectively. The evolution of the grain-grain
 210 contact area (and grain contact stress) with porosity ϕ is described by the porosity function $f_i(\phi)$ ⁶⁷. For dissolution controlled
 211 pressure solution creep, this function takes the following form^{33,66}:

$$f_1(\phi) = \frac{\phi_c}{\phi_c - \phi} \quad (2a)$$

$$f_2(\phi) = \frac{\phi - \phi_0}{\phi_c - \phi} \quad (2b)$$

212 where ϕ_0 is a lower cut-off porosity corresponding to the percolation threshold for an interconnected pore network of 3%⁶⁸, and
 213 ϕ_c is the maximum attainable porosity of a purely dilatant gouge material, referred to here as the ‘critical state’ porosity^{39,69}.
 214 Typically, a porosity function similar to $f_1(\phi)$ is used in analytical models for intergranular pressure solution that employ a
 215 porosity function^{66,67}. However, in laboratory compaction test it has been observed that microphysical model predictions for
 216 compaction by pressure solution overestimate experimentally measured strain rates at low porosities ($< 20\%$), sometimes by
 217 several orders of magnitude⁶⁵. While the physical mechanisms behind this discrepancy are yet to be fully identified, the trends in
 218 the experimental data can be approximated by the modified porosity function $f_2(\phi)$, which asymptotically reduces $\dot{\epsilon}_{ps}$ to zero
 219 for $\phi \rightarrow \phi_0$. Furthermore, this ensures that $\phi > \phi_0$ at all times, preventing negative porosities that are physically unrealistic.
 220 By contrast, shear creep accommodated by pressure solution does not involve volume changes (i.e. porosity reduction), so it is
 221 expected that $\dot{\gamma}_{ps} > 0$ even for $\phi = \phi_0$. A functional form like $f_1(\phi)$ is therefore more likely to describe shear creep by pressure
 222 solution, as is adopted for this study.

223 The constitutive relations for granular flow have been derived as³⁴:

$$\dot{\gamma}_{gr} = \dot{\gamma}_{gr}^* \exp\left(\frac{\tau [1 - \tilde{\mu}^* \tan \psi] - \sigma [\tilde{\mu}^* + \tan \psi]}{\tilde{a} [\sigma + \tau \tan \psi]}\right) \quad (3a)$$

$$\dot{\epsilon}_{gr} = -\tan \psi \dot{\gamma}_{gr} \quad (3b)$$

224 In these relations, $\dot{\gamma}_{gr}$ and $\dot{\epsilon}_{gr}$ denote the granular flow strain rates tangential and normal to the fault plain, respectively, and $\tan \psi$
 225 denotes the average grain-grain dilatation angle, which can be written as $\tan \psi = 2H(\phi_c - \phi)$, where H is a geometric constant of
 226 order 1^{39,69}. The microscopic coefficient of friction of grain-grain contacts is given by ref. 34 as $\tilde{\mu} = \tilde{\mu}^* + \tilde{a} \ln(\dot{\gamma}_{gr}/\dot{\gamma}_{gr}^*)$, $\tilde{\mu}^*$ being
 227 a reference value of $\tilde{\mu}$ evaluated at $\dot{\gamma}_{gr}^*$, and \tilde{a} being the coefficient of logarithmic rate-dependence of $\tilde{\mu}$.

228 With the above constitutive relations for the relevant deformation mechanisms, the evolution of the macroscopic shear stress
 229 and gouge porosity of a zero-dimensional (spring-block) fault can be expressed in the following set of differential equations³⁴:

$$\frac{d\tau}{dt} = k(V_{imp} - h[\dot{\gamma}_{gr} + \dot{\gamma}_{ps}]) \quad (4a)$$

$$\frac{d\phi}{dt} = -(1 - \phi)(\dot{\epsilon}_{gr} + \dot{\epsilon}_{ps}) \quad (4b)$$

230 in which k is the effective shear stiffness (units: Pa m⁻¹) of the fault. The instantaneous fault slip velocity V is obtained from the
 231 addition of the strain rates of granular flow and pressure solution (i.e. $V = h[\dot{\gamma}_{gr} + \dot{\gamma}_{ps}]$).

232 One important characteristic to note, is that the steady-state velocity-dependence of friction, i.e. a material being velocity-
 233 strengthening or -weakening, changes with velocity (see Fig. 1b). As a result, classical rate-and-state friction is only comparable to
 234 the CNS model near steady-state conditions⁶², i.e. for small velocity perturbations around steady-state for which the velocity-
 235 dependence ($a - b$) can be approximated to be constant, so that the steady-state friction is proportional to $\log(V)$. With increasing
 236 departure from steady-state, both model frameworks predict different frictional behaviour, as is notably seen in seismic cycle
 237 simulations³³.

238 Finally, the adopted rheological model currently does not feature any high-velocity dynamic weakening mechanisms (see
 239 e.g. ref. 70). In the absence of dynamic weakening, the coseismic stress drop and maximum slip velocity as produced by the
 240 simulations are likely of smaller magnitude than anticipated for earthquakes in nature, where such mechanisms are known to
 241 operate. Accordingly, afterslip and interseismic creep likely constitute a larger portion of the total slip budget in the simulations
 242 than in nature. Since this study considers the effect of rheological transitions on the nucleation of seismic events (during which
 243 dynamic weakening is inactive), we leave such an extension of the currently adopted model rheology for future studies.

244 **Description of the boundary element method.** To model spatio-temporal variations of fault slip, we employ the boundary
 245 element code QDYN⁴⁰. This seismic cycle simulator originally utilises rate-and-state friction to describe the model fault rheology,
 246 but it has been extended³³ to include the CNS microphysical model as described above. Regardless of the underlying rheological
 247 model, the shear stress at point i on the fault is obtained using the quasi-dynamic approximation⁷¹:

$$\tau_i(t) = -K_{ij} [d_j(t) - d_{imp}] - \eta V_i(t) \quad (5)$$

248 Here, K_{ij} is a stress transfer kernel whose coefficients represent the shear stress induced on the i -th fault element by unitary slip
 249 on the j -th fault element, d_j is the total fault slip on the j -th fault element, and d_{imp} is the far-field displacement, accumulating as
 250 $d_{imp} = V_{imp} \times t$. Radiation damping due to seismic wave radiation normal to the fault plane is accounted for by the last term on
 251 the right-hand side, in which the damping factor η assumes a value of $G/2c_s$, with G being the shear modulus of the homogeneous
 252 elastic medium, and c_s the shear wave speed⁷¹. The stress transfer kernel K_{ij} is computed using a “2.5D” approximation for
 253 infinite one-dimensional faults embedded in two-dimensional homogeneous media (see ref. 24), and fault stresses are obtained via
 254 the spectral approach in finite-size domains⁷². For numerical implementation, Eqn. 5 is differentiated with respect to time to give:

$$\frac{d\tau_i}{dt} = -K_{ij} [V_j(t) - V_{imp}] - \eta \frac{dV_i(t)}{dt} \quad (6)$$

255 The fault slip velocity $V(t)$ is obtained as a function of stress and porosity as $V(\tau, \sigma, \phi) = h [\dot{\gamma}_{gr}(\tau, \sigma, \phi) + \dot{\gamma}_{ps}(\tau, \phi)]$. The
 256 acceleration term on right hand side of Eqn. (6) is then decomposed in its partial derivatives as:

$$\frac{dV}{dt} = \frac{\partial V}{\partial \tau} \frac{d\tau}{dt} + \frac{\partial V}{\partial \phi} \frac{d\phi}{dt} \quad (7a)$$

$$\frac{\partial V}{\partial \tau} = h \left(A \frac{I_s \Omega}{dRT} f_1(\phi) + \dot{\gamma}_{gr} \left[\frac{1 - \bar{\mu} \tan \psi}{\bar{a}(\sigma + \tau \tan \psi)} \right] \right) \quad (7b)$$

$$\frac{\partial V}{\partial \phi} = h \left(\frac{\dot{\gamma}_{ps}}{\phi_c - \phi} + \dot{\gamma}_{gr} \left[\frac{2H(\sigma + \bar{\mu}\tau)}{\bar{a}(\sigma + \tau \tan \psi)} \right] \right) \quad (7c)$$

257 Note that these partial derivatives are given specifically for the assumed porosity functions (Eqn. (2)). Substitution of (7) into (6),
 258 and rearrangement gives:

$$\frac{d\tau_i}{dt} = \frac{-K_{ij} [V_j - V_{imp}] - \eta \frac{\partial V_i}{\partial \phi} \frac{d\phi_i}{dt}}{1 + \eta \frac{\partial V_i}{\partial \tau}} \quad (8a)$$

$$\frac{d\phi_i}{dt} = -(1 - \phi_i) (\dot{\epsilon}_{gr,i} + \dot{\epsilon}_{ps,i}) \quad (8b)$$

259 These equations are of the general form $\dot{\mathbf{X}} = \mathbf{F}(\mathbf{X}, t)$, with $\mathbf{X}(t)$ being a vector containing the collection of $\tau_i(t)$ and $\phi_i(t)$ variables
 260 on all fault elements. This system of ordinary differential equations is solved by the 4(5)th-order Runge-Kutta-Fehlberg method
 261 with adaptive time stepping^{73,74}, as to maintain a relative error of $< 10^{-5}$.

262 **Rendering the heterogeneous fault structure.** By employing a microphysical model that contains microstructural information,
 263 one can closely relate the model fault geometry to field and laboratory observations. In this work, guided by numerous field reports,
 264 we define heterogeneity through spatial variations in pressure solution kinetics, which reflect contrasts in fault rock composition or
 265 spatial variations in strain rate. Following ref. 41, we assume that competent lenses (the asperities) obey a power-law distribution
 266 in size, i.e.:

$$F_X(x) = 1 - cx^{-D} \quad (9)$$

267 where F_X is the cumulative size distribution of asperity size X , D is the fractal dimension (or power-law exponent), and c is a
 268 proportionality constant. Strictly speaking, this cumulative distribution function does not exist for $D > 0$ on an infinite domain,
 269 but it can be re-defined based on a re-scaled probability density function integrated over a finite range of $0 < x_{min} \leq X \leq x_{max}$

270 and $D \neq 0$, which yields:

$$f'_X(x) = \frac{-Dx^{-D-1}}{x_{max}^{-D} - x_{min}^{-D}} \quad (10a)$$

$$F'_X(x) = \int_{x_{min}}^x f'_X(x)dx = \frac{x^{-D} - x_{min}^{-D}}{x_{max}^{-D} - x_{min}^{-D}} \quad (10b)$$

271 In accordance with the above relations, the realisation of the asperity size distribution x can be generated from a uniform variate
272 \hat{X} as:

$$x = \left(x_{min}^{-D} + \left[x_{max}^{-D} - x_{min}^{-D} \right] \hat{X} \right)^{-1/D} \quad (11)$$

273 The procedure to render a fault with the desired statistical properties is then as follows:

- 274 1. First, the discrete asperity size distribution x_i is realised in accordance with Eqn. (11), with x_{min} corresponding to twice
275 the fault element size, and $x_{max} = L$. Between simulations, D is systematically varied between 1 and 2, following the
276 phacoid fractal dimensions reported by ref. 41;
- 277 2. Next, a second size distribution (y_i) is realised that represents the spacing between neighbouring asperities, assuming that
278 the “gaps” between asperities obey the same power-law distribution;
- 279 3. In order to realise the desired asperity occupation ratio f , x_i is multiplied by $f/(1-f)$ (i.e. the ratio of total asperity
280 length over total matrix length) before being combined in an arrangement with y_i ;
- 281 4. The spatial distribution of Z_{ps} for the asperities and the matrix is then sampled from a piece-wise alternating arrangement
282 of x_i and y_i , respectively, where i ranges from 1 to N , so that $\sum_{i=1}^N (x_i + y_i) \geq L$. In other words, the spatial layout of the
283 fault follows an arrangement $x_1, y_1, x_2, y_2, \dots, x_N, y_N$;

284 Owing to the fault’s finite size, stochastic noise causes some variability in the statistical properties of the fault geometry, e.g. by
285 randomly introducing one excessively large asperity, which skews the asperity size distribution. To prevent this, we compare each
286 realised asperity size distribution with the expected distribution (Eqn. (10b)), and the realised value of f with the one that is
287 requested. For large ($> 5\%$) deviations of the size distribution and f from the expected values, the rendered fault structure is
288 rejected and a new one generated.

289 From the above procedure, we obtain a fault structure that is consistent with our interpretation of the field observations
290 summarised in Supplementary Information S3 (see also Fig. 1). This fault geometry is projected onto a one-dimensional periodic
291 fault, and the fault is subjected to down-dip conditions of $V_{imp} = 10^{-9} \text{ m s}^{-1}$ and $\sigma = 50 \text{ MPa}$. For the kinetics of pressure solution
292 Z_{ps} defining the asperity and the matrix, we adopt values of 5×10^{-16} and $3 \times 10^{-15} \text{ Pa}^{-1} \text{ s}^{-1}$. A value of $Z_{ps} = 3 \times 10^{-15} \text{ Pa}^{-1} \text{ s}^{-1}$
293 corresponds to theoretical estimates of Z_{ps} for monomineralic quartz at 250°C and a grain size of $5 \mu\text{m}$ ⁶⁵. The simulation is then
294 run for at least 2,000 years.

295 References

- 296 [1] Benedetti, L. *et al.* Earthquake synchrony and clustering on Fucino faults (Central Italy) as revealed from in situ 36 Cl
297 exposure dating. *Journal of Geophysical Research: Solid Earth* **118**, 4948–4974 (2013).
- 298 [2] Philibosian, B. *et al.* Earthquake supercycles on the Mentawai segment of the Sunda megathrust in the seventeenth century
299 and earlier. *Journal of Geophysical Research: Solid Earth* **122**, 642–676 (2017).
- 300 [3] Ratzov, G. *et al.* Holocene turbidites record earthquake supercycles at a slow-rate plate boundary. *Geology* **43**, 331–334
301 (2015).
- 302 [4] Sieh, K. *et al.* Earthquake Supercycles Inferred from Sea-Level Changes Recorded in the Corals of West Sumatra. *Science*
303 **322**, 1674–1678 (2008).
- 304 [5] Goldfinger, C. *et al.* Turbidite Event History — Methods and Implications for Holocene Paleoseismicity of the Cascadia
305 Subduction Zone. *U.S. Geological Survey Professional Paper 1661-F* 170 (2012).

- 306 [6] Goldfinger, C., Ikeda, Y., Yeats, R. S. & Ren, J. Superquakes and Supercycles. *Seismological Research Letters* **84**, 24–32
307 (2013).
- 308 [7] Mannen, K. *et al.* History of ancient megathrust earthquakes beneath metropolitan Tokyo inferred from coastal lowland
309 deposits. *Sedimentary Geology* (2017).
- 310 [8] Satake, K. Geological and historical evidence of irregular recurrent earthquakes in Japan. *Philosophical Transactions of the*
311 *Royal Society A: Mathematical, Physical and Engineering Sciences* **373**, 20140375 (2015).
- 312 [9] Stevens, V. L. & Avouac, J.-P. Millenary $M > 9.0$ earthquakes required by geodetic strain in the Himalaya. *Geophysical*
313 *Research Letters* **43**, 1118–1123 (2016).
- 314 [10] Satake, K. & Fujii, Y. Review: Source Models of the 2011 Tohoku Earthquake and Long-Term Forecast of Large Earthquakes.
315 *Journal of Disaster Research* **9**, 272–280 (2014).
- 316 [11] Ruff, L. & Kanamori, H. Seismicity and the subduction process. *Physics of the Earth and Planetary Interiors* **23**, 240–252
317 (1980).
- 318 [12] Satake, K. & Atwater, B. F. Long-Term Perspectives on Giant Earthquakes and Tsunamis at Subduction Zones *. *Annu.*
319 *Rev. Earth Planet. Sci* **35**, 349–74 (2007).
- 320 [13] Kagan, Y. Y. Seismic moment-frequency relation for shallow earthquakes: Regional comparison. *Journal of Geophysical*
321 *Research: Solid Earth* **102**, 2835–2852 (1997).
- 322 [14] McCaffrey, R. Global frequency of magnitude 9 earthquakes. *Geology* **36**, 263 (2008).
- 323 [15] Weng, H. & Yang, H. Seismogenic width controls aspect ratios of earthquake ruptures. *Geophysical Research Letters* **44**,
324 2725–2732 (2017).
- 325 [16] Ohta, Y., Freymueller, J., Hreinsdottir, S. & Suito, H. A large slow slip event and the depth of the seismogenic zone in the
326 south central Alaska subduction zone. *Earth and Planetary Science Letters* **247**, 108–116 (2006).
- 327 [17] Gombert, J. Slow-slip phenomena in Cascadia from 2007 and beyond: A review. *Geological Society of America Bulletin* **122**,
328 963–978 (2010).
- 329 [18] Ide, S. The proportionality between relative plate velocity and seismicity in subduction zones. *Nature Geoscience* **6**, 780–784
330 (2013).
- 331 [19] Bécél, A. *et al.* Tsunamigenic structures in a creeping section of the Alaska subduction zone. *Nature Geoscience* **10**, 609–613
332 (2017).
- 333 [20] Noda, H. & Lapusta, N. Stable creeping fault segments can become destructive as a result of dynamic weakening. *Nature*
334 **493**, 518–521 (2013).
- 335 [21] Witter, R. C. *et al.* Unusually large tsunamis frequent a currently creeping part of the Aleutian megathrust. *Geophysical*
336 *Research Letters* **43**, 76–84 (2016).
- 337 [22] Kaneko, Y., Avouac, J. & Lapusta, N. Towards inferring earthquake patterns from geodetic observations of interseismic
338 coupling. *Nature Geoscience* **3**, 363–369 (2010).
- 339 [23] Hillers, G., Ben-Zion, Y. & Mai, P. M. Seismicity on a fault controlled by rate- and state-dependent friction with spatial
340 variations of the critical slip distance. *Journal of Geophysical Research* **111**, B01403 (2006).
- 341 [24] Luo, Y. & Ampuero, J.-P. Stability and effective friction of faults with heterogeneous friction properties and fluid pressure.
342 *Tectonophysics* (2017).

- 343 [25] Tse, S. T. & Rice, J. R. Crustal earthquake instability in relation to the depth variation of frictional slip properties. *Journal*
344 *of Geophysical Research* **91**, 9452 (1986).
- 345 [26] Dieterich, J. H. Modeling of rock friction: 1. Experimental results and constitutive equations. *Journal of Geophysical Research*
346 **84**, 2161 (1979).
- 347 [27] Dieterich, J. H. Time-dependent friction in rocks. *Journal of Geophysical Research* **77**, 3690–3697 (1972).
- 348 [28] Carpenter, B., Collettini, C., Viti, C. & Cavallo, A. The influence of normal stress and sliding velocity on the frictional
349 behaviour of calcite at room temperature: insights from laboratory experiments and microstructural observations. *Geophysical*
350 *Journal International* **205**, 548–561 (2016).
- 351 [29] den Hartog, S., Niemeijer, A. & Spiers, C. New constraints on megathrust slip stability under subduction zone P–T conditions.
352 *Earth and Planetary Science Letters* **353–354**, 240–252 (2012).
- 353 [30] Niemeijer, A. R. & Spiers, C. J. Velocity dependence of strength and healing behaviour in simulated phyllosilicate-bearing
354 fault gouge. *Tectonophysics* **427**, 231–253 (2006).
- 355 [31] Shimamoto, T. Transition Between Frictional Slip and Ductile Flow for Halite Shear Zones at Room Temperature. *Science*
356 **231**, 711–714 (1986).
- 357 [32] Verberne, B. A. *et al.* Microscale cavitation as a mechanism for nucleating earthquakes at the base of the seismogenic zone.
358 *Nature Communications* **8**, 1645 (2017).
- 359 [33] van den Ende, M., Chen, J., Ampuero, J.-P. & Niemeijer, A. A comparison between rate-and-state friction and microphysical
360 models, based on numerical simulations of fault slip. *Tectonophysics* (2017).
- 361 [34] Chen, J. & Spiers, C. J. Rate and state frictional and healing behavior of carbonate fault gouge explained using microphysical
362 model. *Journal of Geophysical Research: Solid Earth* 1–42 (2016).
- 363 [35] den Hartog, S. A. M. & Spiers, C. J. A microphysical model for fault gouge friction applied to subduction megathrusts.
364 *Journal of Geophysical Research: Solid Earth* **119**, 1510–1529 (2014).
- 365 [36] Brechet, Y. & Estrin, Y. The effect of strain rate sensitivity on dynamic friction of metals. *Scripta metallurgica et materialia*
366 **30**, 1449–1454 (1994).
- 367 [37] Perfettini, H. & Molinari, A. A Micromechanical Model of Rate and State Friction: 1. Static and Dynamic Sliding. *Journal*
368 *of Geophysical Research: Solid Earth* (2017).
- 369 [38] Aharonov, E. & Scholz, C. H. A physics-based rock-friction constitutive law: steady-state friction. *Journal of Geophysical*
370 *Research: Solid Earth* (2017).
- 371 [39] Niemeijer, A. R. & Spiers, C. J. A microphysical model for strong velocity weakening in phyllosilicate-bearing fault gouges.
372 *Journal of Geophysical Research* **112**, B10405 (2007).
- 373 [40] Luo, Y., Ampuero, J.-P., Galvez, P., Van den Ende, M. & Idini, B. QDYN: a Quasi-DYNAMIC earthquake simulator (v1.1)
374 (2017).
- 375 [41] Fagereng, Å. Geology of the seismogenic subduction thrust interface. *Geological Society, London, Special Publications* **359**,
376 55–76 (2011).
- 377 [42] Holdsworth, R. *et al.* Fault rocks from the SAFOD core samples: Implications for weakening at shallow depths along the San
378 Andreas Fault, California. *Journal of Structural Geology* **33**, 132–144 (2011).

- 379 [43] Jefferies, S. *et al.* The nature and importance of phyllonite development in crustal-scale fault cores: an example from the
380 Median Tectonic Line, Japan. *Journal of Structural Geology* **28**, 220–235 (2006).
- 381 [44] Smeraglia, L. *et al.* Microstructural evidence for seismic and aseismic slips along clay-bearing, carbonate faults. *Journal of*
382 *Geophysical Research: Solid Earth* (2017).
- 383 [45] Chester, F. M. & Higgs, N. G. Multimechanism friction constitutive model for ultrafine quartz gouge at hypocentral conditions.
384 *Journal of Geophysical Research: Solid Earth* **97**, 1859–1870 (1992).
- 385 [46] Niemeijer, A. R. & Vissers, R. L. Earthquake rupture propagation inferred from the spatial distribution of fault rock frictional
386 properties. *Earth and Planetary Science Letters* **396**, 154–164 (2014).
- 387 [47] Rowe, C. D., Meneghini, F. & Moore, J. C. Textural record of the seismic cycle: strain-rate variation in an ancient subduction
388 thrust. *Geological Society, London, Special Publications* **359**, 77–95 (2011).
- 389 [48] Hickman, S. H. & Evans, B. Kinetics of pressure solution at halite-silica interfaces and intergranular clay films. *Journal of*
390 *Geophysical Research* **100**, 13113 (1995).
- 391 [49] Ellsworth, W. L. & Beroza, G. C. Seismic Evidence for an Earthquake Nucleation Phase. *Science* **268**, 851–855 (1995).
- 392 [50] Chen, K. H. & Bürgmann, R. Creeping faults: Good news, bad news? *Reviews of Geophysics* **55**, 282–286 (2017).
- 393 [51] Tsutsumi, A. & Shimamoto, T. High-velocity frictional properties of gabbro. *Geophysical Research Letters* **24**, 699–702
394 (1997).
- 395 [52] Proctor, B. P. *et al.* Dynamic weakening of serpentinite gouges and bare surfaces at seismic slip rates. *Journal of Geophysical*
396 *Research: Solid Earth* **119**, 8107–8131 (2014).
- 397 [53] Hori, T. & Miyazaki, S. A possible mechanism of M 9 earthquake generation cycles in the area of repeating M 7 $\bar{8}$ earthquakes
398 surrounded by aseismic sliding. *Earth, Planets and Space* **63**, 773–777 (2011).
- 399 [54] Michel, S., Avouac, J.-P., Lapusta, N. & Jiang, J. Pulse-like partial ruptures and high-frequency radiation at creeping-locked
400 transition during megathrust earthquakes. *Geophysical Research Letters* **44**, 8345–8351 (2017).
- 401 [55] Noda, H., Nakatani, M. & Hori, T. Large nucleation before large earthquakes is sometimes skipped due to cascade-up-
402 Implications from a rate and state simulation of faults with hierarchical asperities. *Journal of Geophysical Research: Solid*
403 *Earth* **118**, 2924–2952 (2013).
- 404 [56] Reinen, L. A., Tullis, T. E. & Weeks, J. D. Two-mechanism model for frictional sliding of serpentinite. *Geophysical Research*
405 *Letters* **19**, 1535–1538 (1992).
- 406 [57] Sibson, R. H. Fault zone models, heat flow, and the depth distribution of earthquakes in the continental crust of the United
407 States. *Bulletin of the Seismological Society of America* **72**, 151–163 (1982).
- 408 [58] Noda, H. & Shimamoto, T. Transient behavior and stability analyses of halite shear zones with an empirical rate-and-state
409 friction to flow law. *Journal of Structural Geology* **38**, 234–242 (2012).
- 410 [59] Shimamoto, T. & Noda, H. A friction to flow constitutive law and its application to a 2-D modeling of earthquakes. *Journal*
411 *of Geophysical Research: Solid Earth* **119**, 8089–8106 (2014).
- 412 [60] Beeler, N. M. Constructing Constitutive Relationships for Seismic and Aseismic Fault Slip. *Pure and Applied Geophysics*
413 **166**, 1775–1798 (2009).
- 414 [61] Chen, J. & Niemeijer, A. R. Seismogenic Potential of a Gouge-filled Fault and the Criterion for Its Slip Stability: Constraints
415 From a Microphysical Model. *Journal of Geophysical Research: Solid Earth* **122**, 9658–9688 (2017).

- 416 [62] Chen, J., Niemeijer, A. R. & Spiers, C. J. Microphysically derived expressions for rate-and-state friction parameters, a , b ,
417 and D . *Journal of Geophysical Research: Solid Earth* (2017).
- 418 [63] Atkinson, B. K. Subcritical crack growth in geological materials. *Journal of Geophysical Research* **89**, 4077 (1984).
- 419 [64] Brantut, N., Heap, M. J., Meredith, P. G. & Baud, P. Time-dependent cracking and brittle creep in crustal rocks: A review.
420 *Journal of Structural Geology* **52**, 17–43 (2013).
- 421 [65] Niemeijer, A. R., Spiers, C. J. & Bos, B. Compaction creep of quartz sand at 400-600C: experimental evidence for
422 dissolution-controlled pressure solution. *Earth and Planetary Science Letters* **195**, 261–275 (2002).
- 423 [66] Pluymakers, A. M. H. & Spiers, C. J. Compaction creep of simulated anhydrite fault gouge by pressure solution: theory v.
424 experiments and implications for fault sealing. *Geological Society, London, Special Publications* **409**, 107–124 (2014).
- 425 [67] Spiers, C. J., De Meer, S., Niemeijer, A. R. & Zhang, X. Kinetics of rock deformation by pressure solution and the role of
426 thin aqueous films. In Nakashima, S., Spiers, C. J., Mercury, L., Fenter, P. A. & Hochella, M. F. J. (eds.) *Physicochemistry*
427 *of Water in Geological and Biological Systems*, 129–158 (Universal Academy Press, Tokyo, 2004).
- 428 [68] van der Marck, S. C. Network Approach to Void Percolation in a Pack of Unequal Spheres. *Physical Review Letters* **77**,
429 1785–1788 (1996).
- 430 [69] Paterson, M. S. A theory for granular flow accommodated by material transfer via an intergranular fluid. *Tectonophysics*
431 **245**, 135–151 (1995).
- 432 [70] Tullis, T. Friction of Rock at Earthquake Slip Rates. In *Treatise on Geophysics*, vol. 4, 131–152 (Elsevier, 2007).
- 433 [71] Rice, J. R. Spatio-temporal complexity of slip on a fault. *Journal of Geophysical Research* **98**, 9885 (1993).
- 434 [72] Cochard, A. & Rice, J. R. A spectral method for numerical elastodynamic fracture analysis without spatial replication of the
435 rupture event. *Journal of the Mechanics and Physics of Solids* **45**, 1393–1418 (1997).
- 436 [73] Fehlberg, E. Low-Order Classical Runge-Kutta Formulas with Step-Size Control and Their Application to some Heat-Transfer
437 Problems. *NASA Technical Report* **315** (1969).
- 438 [74] Shampine, L. F., Watts, H. A. & Davenport, S. M. Solving Nonstiff Ordinary Differential Equations - The State of the Art.
439 *SIAM Review* **18**, 376–411 (1976).
- 440 [75] Van den Ende, M. P. A. Input scripts of seismic cycle simulations of heterogeneous faults. *GFZ Data Services* (2018).

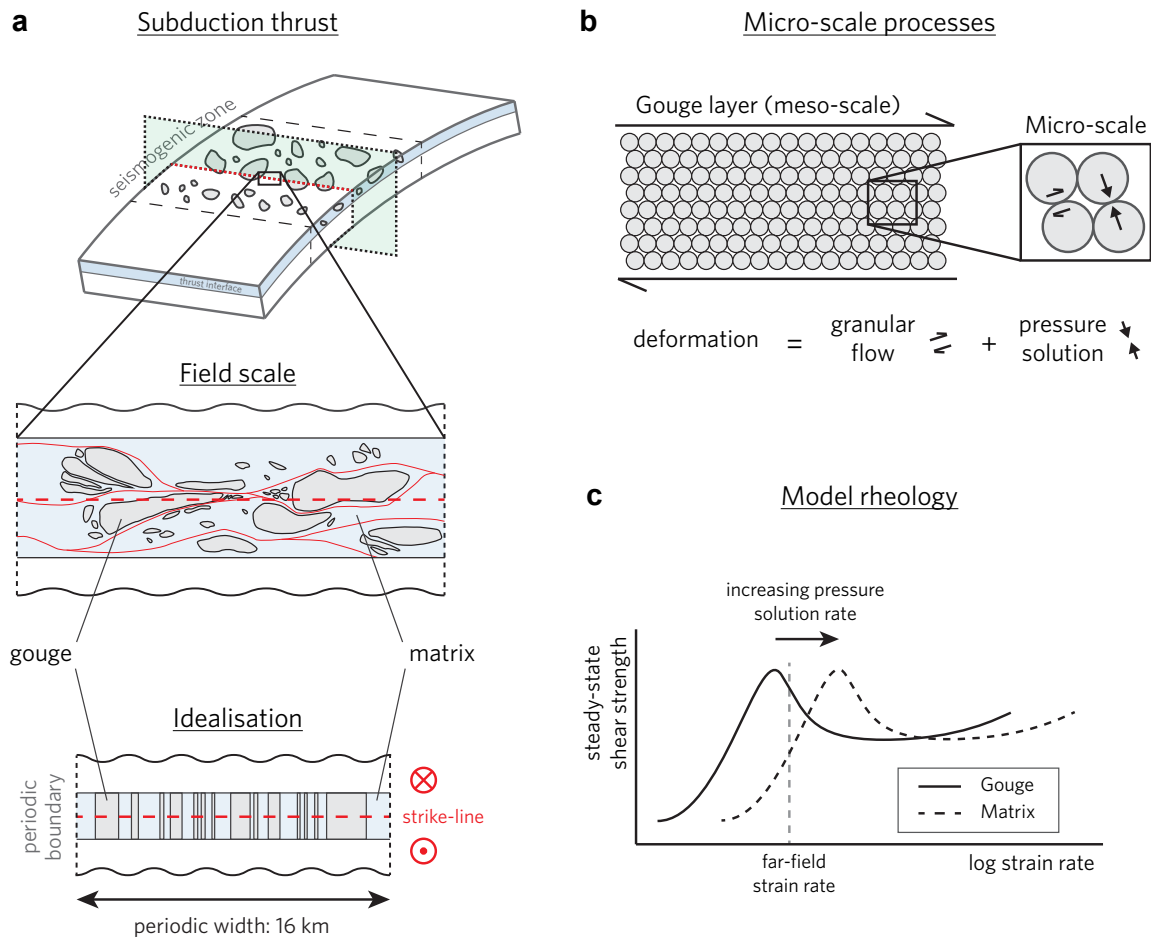


Figure 1 Properties of the model fault. **a**, Idealisation of the envisioned fault geometry, after Fagereng⁴¹. **b**, Assumed microstructure and micro-processes (granular flow and pressure solution). **c**, Schematic diagram of the steady-state shear strength versus strain rate, as predicted by the CNS microphysical model. The compositional variation along the fault is reflected by a contrast in pressure solution kinetics, causing a relative shift of the steady-state strength curves.

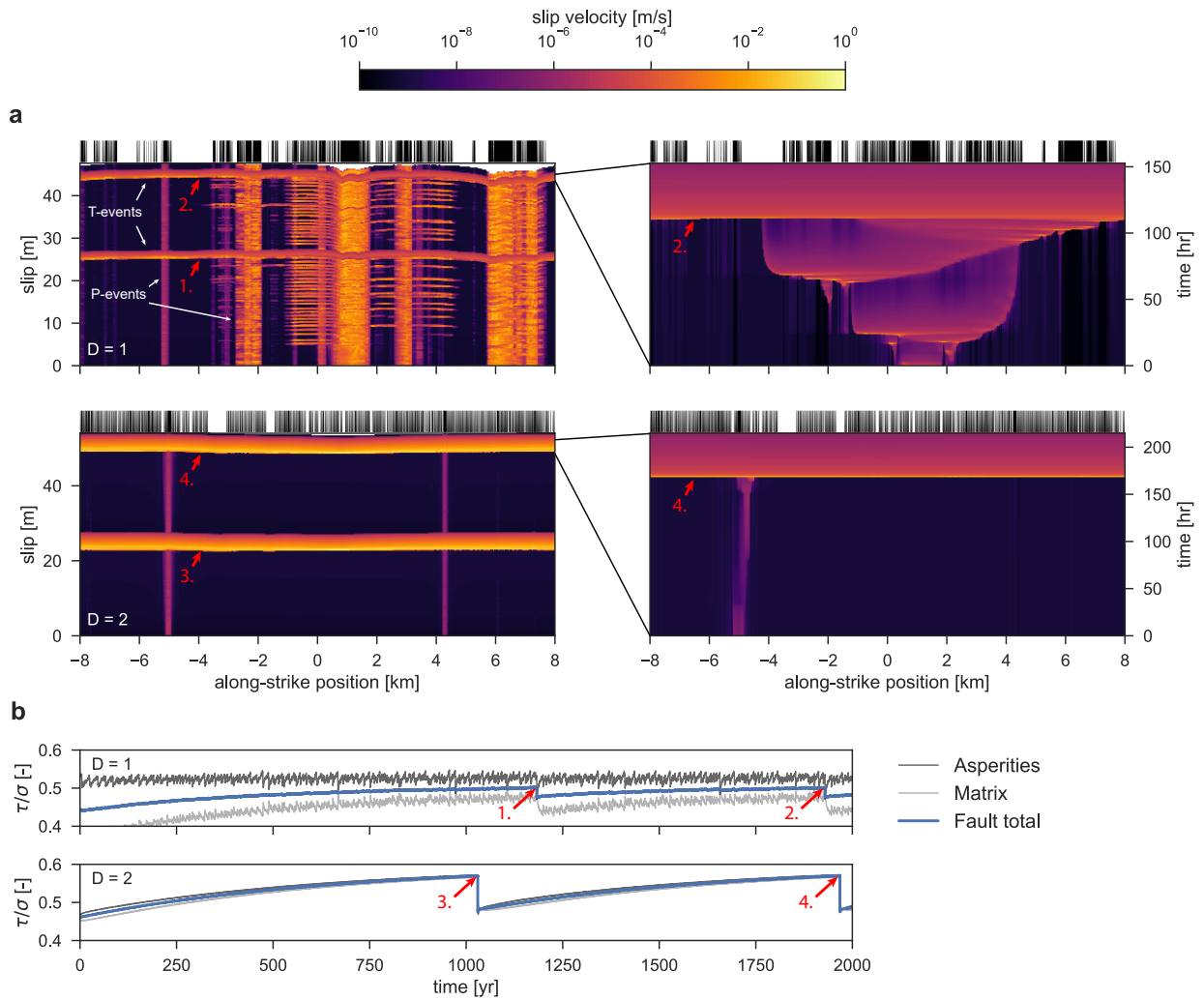


Figure 2 Examples of model fault behaviour. **a**, Spatio-temporal distribution of fault slip velocity (left panels) and nucleation of the last T-instability in each simulation (right panels). The fractal dimension D is as indicated. P-instabilities are identified as small 'hot' regions that span only a portion of the fault, whereas T-instabilities span the entire fault. For reference, the seismogenic asperity distribution is indicated by the black bars at the top of each panel. Simulations with $D = 1$ show numerous regular earthquakes controlled by the local asperity distribution, and a cascade-up style of nucleation of a T-instability. Simulations with $D = 2$ exhibits only minute slow slip events during the interseismic period of a T-event, which emerges with no precursory activity from a small nucleus. **b**, Time-series of the average stress supported by the asperities, the matrix, and the fault as a whole, for $D = 1$ and $D = 2$. A T-instability is triggered when the stress supported by the matrix reaches a critical value. The red coloured numbers in this figure serve to identify unique T-events across the different panels.

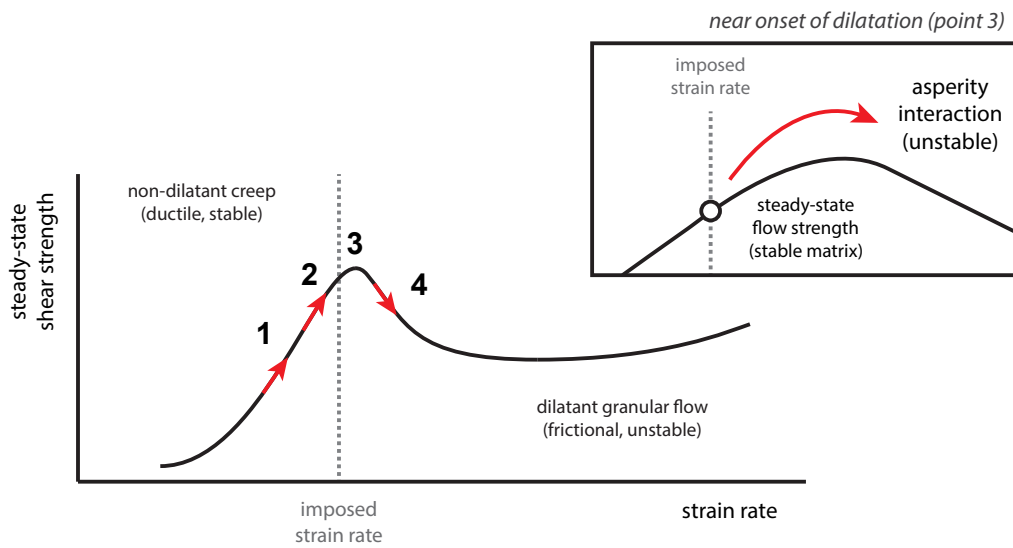


Figure 3 Synoptic overview of the nucleation process. The steady-state strength profile of the matrix, as a function of strain rate, is characterised by a transition from non-dilatant ductile creep (stable) to dilatant granular flow (unstable). At a given moment in time, the stress supported by the matrix is indicated by point 1. Due to tectonic loading and non-uniform fault slip, the stress on the matrix increases (point 2). At a critical value of stress, the matrix enters the dilatant granular flow regime, and a T-instability nucleates.